INTERNATIONAL JOURNAL FOR NUMERICAL METHODS IN FLUIDS
Int. J. Numer. Meth. Fluids 2001; **37**: 321–339 (DOI: 10.1002/fld.176)

Theory and applications in stability of free-surface time-domain boundary element models

Bjarne Büchmann*,[1]

Department of Hydrodynamics and Water Resources, Technical University of Denmark, Lyngby, Denmark

SUMMARY

A method is presented for examining the stability of a free-surface time-domain boundary element model based on B-splines. Effects of a non-uniform discretization occurring in practical applications are included. It is demonstrated that instabilities may occur, even in situations where earlier stability analyses predicted the scheme to be stable. These instabilities are due to non-uniformities in the spatial discretization, which have until now not been included in the stability analyses. Copyright © 2001 John Wiley & Sons, Ltd.

KEY WORDS: B-splines; boundary element method; higher-order basis functions; stability analysis; three-dimensional; time-domain

1. INTRODUCTION

Since the first papers were published where boundary element methods (BEMs) were used for modelling of free-surface waves in the time domain (see e.g. Longuet-Higgins and Cokelet [1]), short-wave instabilities (so-called 'wiggles' or 'saw-tooth instabilities') have been observed, and various techniques have been used to remedy the problem. Dommermuth and Yue [2] showed that control over the minimum grid size is necessary for stability of the fully non-linear Eulerian–Lagrangian time-domain boundary element models. Thus, 'regridding' techniques are often used to stabilize these models. It should be noted that the smoothing effect of the regridding schemes may well affect waves longer than the grid scale, and that conclusive work on this topic still remains to be done. For the finite-order time-domain methods (see e.g. Isaacson and Cheung [3] and Büchmann *et al.* [4]), the grid does not change in time and thus regridding techniques cannot be used to eliminate instabilities. Furthermore, at least for the finite-order models, the wiggles tend to grow exponentially in time, eventually to dominate any 'physical' waves in the model. Therefore, methods such as 'filtering' or 'smoothing' are often used to deal with short-wave instabilities in finite-order models. However, smoothing and

* Correspondence to: Department of Hydrodynamics and Water Resources, Technical University of Denmark, Building 115-061, DK-2800 Lyngby, Denmark.
[1] E-mail: bjarne@buchmann.dk

Received April 2000
Revised September 2000

filtering are no more than treating the symptoms of an unstable model and thus should be applied with caution. Obviously, it would be better to solve the problem by constructing a stable model where neither smoothing nor filtering is needed to obtain stable results.

In the late 1970s, BEMs with polynomial bases were used to solve two-dimensional linear free-surface problems in the frequency domain, see e.g. Harten and Efrony [5] and Fleron [6]. More recently, higher-order methods have been employed for time-domain calculations, see e.g. Kim *et al.* [7]. Unfortunately, the introduction of a higher-order basis did not solve the instability problems. If anything, the higher-order methods in general are less stable than their lower-order equivalents. As a consequence, some attention has been given to the stability analysis of higher-order time-domain models for the interaction between waves, current and a floating body. Büchmann [8] gives a thorough linear stability analysis of a set of B-spline-based BEMs, extending the work by Vada and Nakos [9] to include effects of finite water depth and current at arbitrary angles with the free-surface grid. The analysis is based on the discrete dispersion relation on a uniform grid on the free surface. The stability conditions obtained are basically of the same form as the Courant condition found by Dommermuth and Yue [2]—only the critical value of the time step size varies between the models. It should be noted, however, that certain time integration schemes may lead to models that are unconditionally unstable. A classical example of this is the fully explicit Euler scheme, which yields unstable solutions for all choices of the time step size.

It was noted by Büchmann [8] that instabilities can be observed in cases where the stability analyses predict the model to be stable. Vada and Nakos [9], and later Kim *et al.* [7], suggest that similar instabilities observed in their models (and not predicted by their stability analysis) are caused by a wave number with zero group velocity (a 'resonant mode'), resulting in a wave where the energy cannot be radiated away. Thus, the instabilities should be caused by the external forcing of the problem. However, a thorough analysis of the discrepancies between the stability analyses and the observed model behaviour is presently lacking.

To illustrate the unstable behaviour and to motivate the analysis of the present work, a particular time series from a linear standing-wave simulation with zero external forcing is given in Figure 1. In the figure, calculated elevations are given as functions of time for three different values of the time step size. According to the existing stability analysis all three time step sizes are smaller than the critical value for the present geometry. As a consequence, all simulations

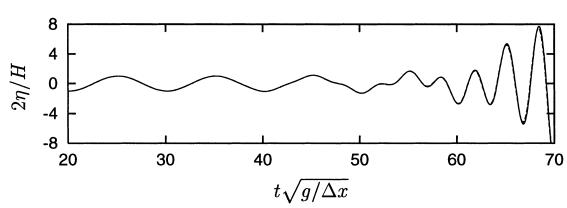

Figure 1. Example of time series of water elevation, η, using three different time step sizes, $\Delta t = \frac{1}{10}\sqrt{\Delta x/g}$ (– – –), $\frac{1}{20}\sqrt{\Delta x/g}$ (- - -), and $\frac{1}{50}\sqrt{\Delta x/g}$ (—), showing a pronounced temporal instability. The water elevation and the time are normalized by the initial wave height H, the gravitational acceleration g and the mesh size Δx.

are *a priori* expected to be stable [8]. However, from Figure 1 it is noted that the model is unstable for all three time-step sizes. In fact, the time series converges temporally to a solution that is unstable in time. Since the problem in this case has zero external forcing, the observed instabilities cannot be accumulation of energy from the forcing of the problem. Therefore, a different explanation must be sought for.

More details on the instability and this particular numerical experiment for which results are given in Figure 1 will be given in the present paper. At present, let the observed instabilities motivate the efforts to study the stability of particular examples of the fully discretized system in detail directly, without the assumptions normally made in a stability analysis. A basic understanding of the origin of these instabilities, which are not predicted by the existing analyses, is important for the development of a stable and reliable method.

2. STABILITY ANALYSIS ASSUMPTIONS

Both the stability analysis performed by Büchmann [8] and the analysis in the current work are made for linear time-domain BEMs. However, the works may also be interpreted as linear analyses for non-linear models.

In a stability analysis of a complex model such as the present, a number of simplifications besides the linearization must be made in order to yield a solvable problem. In the stability analyses presented by Vada and Nakos [9] and by Büchmann [8] a free surface of infinite extent is considered, and neither surface-piercing nor fully submerged bodies are included in the analyses. The infinite free surface is then discretized by a uniform rectangular grid rendering all the basis functions identical except for simple horizontal translations. Linear waves riding on a uniform current over a horizontal sea bed are then considered, and the discrete dispersion relation is found for these waves. The stability properties of a spatial and temporal discretion can then be obtained from the roots of the discrete dispersion relation [8,9]. Even though the resulting problem may seem simple, a rather tedious analysis must be undertaken to actually compute the roots [8].

In practical applications almost all the simplifying assumptions of the stability analyses [8,9] may be violated. In particular, fixed or floating bodies, possibly intersecting the free surface, are examined in practice. The bodies intersecting the free surface then lead to non-uniformity of the free-surface discretization. Further, due to the finite computational power available, the free surface is truncated at some finite distance. This may also lead to non-uniformities. For wave propagation problems non-uniform water depth may also be considered. In essence, the problems considered in engineering applications are much more complicated in nature than the simplified problems considered in the stability analyses presented so far. In the remaining part of the present paper a simpler and numerically more direct method is given for examining the stability of a time-domain free-surface BEM.

3. GOVERNING EQUATIONS

The boundary element methods considered in the present work solve three-dimensional potential flow problems with a free surface in the time domain. Thus, a three-dimensional

irrotational flow in a homogeneous, incompressible and inviscid fluid is considered. Let t denote the time and $\mathbf{x} = (x, y, z)$ the position vector. A velocity potential $\phi(\mathbf{x}, t)$ is defined so that the velicity $\mathbf{u}$ in the three spatial dimensions can be written as

$$\mathbf{u} = \nabla\phi = (\phi_x, \phi_y, \phi_z) \tag{1}$$

where ∇ is the gradient operator and the subscripts x, y and z denote the spatial derivatives in the respective directions. The co-ordinate system is chosen such that $z = 0$ corresponds to the still water level. The continuity equation combined with the condition of an irrotational flow yields the well-known Laplace equation

$$\nabla^2\phi = 0 \tag{2}$$

The Laplace equation is the governing differential equation in the fluid domain bounded by a continuous and piecewise differentiable surface Γ. The boundary Γ is subdivided into a sea bed, Γ_b, a free surface, Γ_f, a (wetted) body surface, Γ_b, and a vertical boundary, Γ_r, truncating the infinite domain as shown in Figure 2. It should be noted that none of these surfaces need be connected. For instance when a so-called moon-pool on an offshore platform is considered, Γ_f will have at least two disjointed surfaces. Similarly, if a multi-hull vessel is considered, Γ_b consists of more than one part.

At the still water level a Stokesian procedure is used to expand the kinematic and dynamic free-surface boundary conditions. The velocity potential is expanded by a perturbation series $\phi = \phi^{(0)} + \varepsilon\phi^{(1)} + \cdots$, where ε is a perturbation parameter relating to the wave steepness, and the superscripts (0) and (1) denote the order of the expansion. The zeroth-order term $\phi^{(0)}$ corresponds to the steady potential induced by a current and includes an incident uniform current and the disturbance of the uniform current due to the presence of the structure. Only a weak current is considered in the present work and thus the steady current potential $\phi^{(0)}$ is determined as the solution to the so-called 'double-body flow' with no steady waves introduced (a rigid-lid condition applied at $z = 0$), since these would be of second order in the current speed. Due to the absence of steady wave elevations ($\eta^{(0)} = 0$), the perturbation series expansion of the free-surface elevation may be written as $\eta = \varepsilon\eta^{(1)} + \cdots$. If the perturbed quantities are introduced into the Taylor-expanded free-surface boundary conditions and if

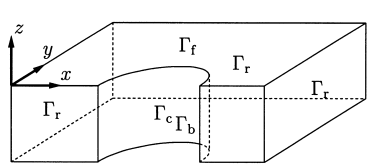

Figure 2. Definition of fluid domain and boundaries. In this figure the xz-plane defines a symmetry plane for the problem.

terms of the same order in ε are collected, then two free-surface boundary conditions are obtained for each order of the solution. The zeroth-order equations simply yield the rigid-lid condition for the steady potential. At first order the conditions read (see e.g. Büchmann *et al.* [4])

$$\eta_t^{(1)} = \phi_{\mathrm{n}}^{(1)} - \phi_x^{(0)}\eta_x^{(1)} - \phi_y^{(0)}\eta_y^{(1)} - \eta^{(1)}(\phi_{xx}^{(0)} + \phi_{yy}^{(0)}) \tag{3}$$

$$\phi_t^{(1)} = -g\eta^{(1)} - \phi_x^{(0)}\phi_x^{(1)} - \phi_y^{(0)}\phi_y^{(1)} \tag{4}$$

Here subscript n denotes partial differentiation along a unit normal vector pointing outwards from the fluid domain. On the linearized free surface $\phi_{\mathrm{n}} = \phi_z$, but the subscript n is preferred to emphasize the connection with the boundary integral equation, which will be introduced later.

In the present work the stability of only the first-order terms will be examined. The equations for the second-order solution are identical to the first-order equations, only with a number of 'forcing terms' depending on the solution at lower order. Since the forcing terms do not influence the stability characteristics of the BEM, the stability properties of the second-order solution are exactly the same as for the first-order solution.

Together with the boundary conditions at the free surface, boundary conditions on the sea bed, on the body and on the truncation boundaries exist. At all these boundaries Neumann conditions specifying the volume flux can be found in the form

$$\phi_{\mathrm{n}} = f(\mathbf{x}, t) \tag{5}$$

It should be noted that Equation (5) is an explicit Neumann condition, i.e. for the present analysis it is assumed that the flux condition on the boundary is known and thus not part of the solution to the problem. Boundary conditions that can be brought to this form include conditions for fixed impermeable boundaries and forced body motions.

When Green's second identity is used, the governing equation (2) in the linearized fluid domain is transformed into a boundary integral equation of the form

$$\alpha(\mathbf{x})\phi^{(p)}(\mathbf{x}, t) = \int_\Gamma G(\mathbf{x}, \boldsymbol{\xi})\phi_{\mathrm{n}}^{(p)}(\boldsymbol{\xi}, t)\,\mathrm{d}\Gamma - \int_\Gamma G_{\mathrm{n}}(\mathbf{x}, \boldsymbol{\xi})\phi^{(p)}(\boldsymbol{\xi}, t)\,\mathrm{d}\Gamma, \quad p = 0, 1 \tag{6}$$

Here $\mathbf{x}$ is an observation point and $\boldsymbol{\xi}$ is a point on the integration path (i.e. $\boldsymbol{\xi}$ is situated at the boundary Γ). The term α is the 'wetted angle' at the observation point $\mathbf{x}$. If $\mathbf{x}$ is on the boundary Γ, then α is given as the interior angle of the boundary at the location $\mathbf{x}$, i.e. $\alpha = 2\pi$ if $\mathbf{x}$ is on a smooth part of the boundary. The kernel function $G(\mathbf{x}, \boldsymbol{\xi})$ is the free space Green's function (also denoted 'simple source' or 'monopole')

$$G(\mathbf{x}, \boldsymbol{\xi}) = \frac{1}{r} = \frac{1}{|\mathbf{r}|} = \frac{1}{|\boldsymbol{\xi} - \mathbf{x}|} \tag{7}$$

where r is defined as the length of the vector $\mathbf{r} = \boldsymbol{\xi} - \mathbf{x}$.

4. DISCRETIZATION OF THE GOVERNING EQUATIONS

In the following section an outline will be given for the time-domain boundary element methods covered by the analysis in the present work. The methods are based on a few equations introduced in the previous section. In particular, Stokesian free-surface boundary conditions (3) and (4), explicit Neumann conditions (5) and the boundary integral equation (6) will be used. These equations form an initial value/boundary value problem, which fully describes the potential flow in the fluid domain.

From the form of the equations it is noted that the variables in the problem are the potential $\phi^{(p)}$ and its normal derivative $\phi_n^{(p)}$ on the entire boundary Γ, and the elevation $\eta^{(p)}$ on the linearized free surface Γ_f. The time-invariant zeroth-order solution needs to be found only once at the beginning of a simulation. However, a new first-order solution ($\phi^{(1)}$, $\phi_n^{(1)}$, $\eta^{(1)}$) must be obtained at each time step. Thus, the employed solution procedure is as follows. At each time step the linear free-surface boundary conditions (3) and (4) are time-integrated to yield $\phi^{(1)}$ and $\eta^{(1)}$ on the free surface. The explicit Neumann boundary conditions are used to obtain $\phi_n^{(1)}$ on the remaining boundaries. For obvious reasons, these boundaries will be denoted 'Neumann boundaries' in the following. Similarly, since $\phi^{(1)}$ is found on the free surface by use of the boundary conditions, each part of the boundary belonging to the free surface may be denoted a 'Dirichlet boundary'. After updating $\phi^{(1)}$ and $\eta^{(1)}$ on the free surface and $\phi_n^{(1)}$ on the Neumann boundaries, the remaining unknowns ($\phi_n^{(1)}$ on the free surface and $\phi^{(1)}$ on the Neumann boundaries) are obtained by use of the boundary integral equation.

The boundary, Γ, of the fluid domain is divided into a number of 'patches', Γ_j, such that the normal vector of the boundary is continuous on each patch. Thus, the geometry is 'smooth' in the interior of each patch. The geometry of each patch is given by a parametric transformation, i.e. as a function of two parameters denoted u and v

$$\mathbf{x} = \mathbf{x}_j(u, v), \quad \mathbf{x} \in \Gamma_j, \quad (u, v) \in [-1{:}1] \times [-1{:}1] \tag{8}$$

The transformation is assumed to be regular in the interior of the patch, such that the Jacobian of the transformation is non-zero there.

At each order p the unknowns on the boundary are described as linear combinations of some basis functions B_j such that

$$\phi^{(p)}(\mathbf{x}, t) = \sum_{j=1}^{N} a_j^{(p)}(t) B_j(\mathbf{x}), \quad \mathbf{x} \in \Gamma \tag{9a}$$

$$\phi_n^{(p)}(\mathbf{x}, t) = \sum_{j=1}^{N} b_j^{(p)}(t) B_j(\mathbf{x}), \quad \mathbf{x} \in \Gamma \tag{9b}$$

$$\eta^{(p)}(\mathbf{x}, t) = \sum_{j=1}^{N} c_j^{(p)}(t) B_j(\mathbf{x}), \quad \mathbf{x} \in \Gamma \tag{9c}$$

Here N is the number of basis functions employed, and the vectors a, b and c are denoted the 'coefficients' of the basis function, which yield ϕ, ϕ_n and η respectively, on the boundary. In the present work, and in the stability analyses by Vada and Nakos [9] and by Büchmann [8], basis functions based on B-splines are employed. The parameters (u, v) introduced in (8) are used for defining the B-spline basis functions on each patch of the boundary. The basis functions are defined as tensor products of one-dimensional B-splines defined in each of the u and v directions. In the stability analyses by Vada and Nakos [9] and by Büchmann [8] it is assumed that all the basis function have the same shape, i.e. that they differ only by horizontal translation. However, in practical models this is not the case. It was shown by Büchmann [10] that the boundary integral equations are fairly well conditioned if multiple knots are used at the patch boundaries and if collocation points are placed at the centroids of the basis functions. As a consequence, it can be an advantage to position multiple knots at the patch boundaries increasing the magnitude of some of the basis functions (see Figure 3). The BEMs that will be examined in this work utilize B-spline-based basis function, multiple knots at the patch boundaries and collocation points positioned at the centroids of the basis functions. However, it should be noted that these are not general restrictions on the analysis, but affect only the particular example discussed in Section 6. In fact, the analysis should be fairly easy to extend to include methods that use other higher-order basis functions than B-splines.

The continuous problem is discretized using basis functions (9) and collocation points. The number of basis functions and collocation points located on the free surface is denoted N_F, while the total number is N.

The first-order kinematic free-surface boundary condition (3) is thus discretized as

$$\begin{aligned}\sum_{j=1}^{N_F} \frac{\partial c_j^{(1)}}{\partial t} B_j(\mathbf{x}_i) = &\sum_{j=1}^{N_F} b_j^{(1)} B_j(\mathbf{x}_i) - \sum_{j=1}^{N_F} a_j^{(0)} \frac{\partial B_j(\mathbf{x}_i)}{\partial x} \sum_{j=1}^{N_F} c_j^{(1)} \frac{\partial B_j(\mathbf{x}_i)}{\partial x} \\ &- \sum_{j=1}^{N_F} a_j^{(0)} \frac{\partial B_j(\mathbf{x}_j)}{\partial y} \sum_{j=1}^{N_F} c_j^{(1)} \frac{\partial B_j(\mathbf{x}_i)}{\partial y} \\ &- \left(\sum_{j=1}^{N_F} a_j^{(0)} \frac{\partial^2 B_j(\mathbf{x}_i)}{\partial x^2} + \sum_{j=1}^{N_F} a_j^{(0)} \frac{\partial^2 B_j(\mathbf{x}_i)}{\partial y^2} \right) \sum_{j=1}^{N_F} c_j^{(1)} B_j(\mathbf{x}_i) \end{aligned} \tag{10}$$

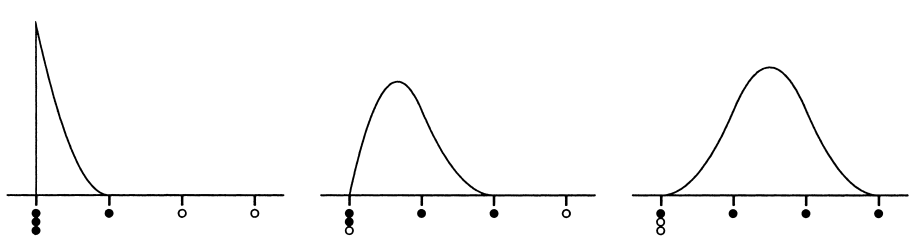

Figure 3. Third-order one-dimensional B-splines defined on a uniform grid, but with a non-uniform defining knot vector. The knots that define each function (●) as well as the remaining knots (○) are shown. Here multiple knots are used at the first grid point.

This equation can for $i = 1, \ldots, N_F$ be rewritten in matrix form as

$$\mathbf{B}c_t^{fs} = \mathbf{B}b^{fs} - \mathbf{A}c^{fs} \tag{11}$$

The superscript fs denotes 'free surface', i.e. a^{fs}, b^{fs} and c^{fs} are vectors of the basis function coefficients on the free surface, each vector being of length N_F. In (11) subscript t denotes differentiation with respect to time, as previously defined, and

$$\mathbf{B}_{ij} = B_j(\mathbf{x}_i) \tag{12}$$

$$\mathbf{A}_{ij} = \frac{\partial \phi^{(0)}(\mathbf{x}_i)}{\partial x}\frac{\partial B_j(\mathbf{x}_i)}{\partial x} + \frac{\partial \phi^{(0)}(\mathbf{x}_i)}{\partial y}\frac{\partial B_j(\mathbf{x}_i)}{\partial y} + \left(\frac{\partial^2 \phi^{(0)}(\mathbf{x}_i)}{\partial x^2} + \frac{\partial^2 \phi^{(0)}(\mathbf{x}_i)}{\partial y^2}\right)B_j(\mathbf{x}_i) \tag{13}$$

It should be noted that the zeroth-order solution $\phi^{(0)}$ may or may not be discretized using the basis functions B_j. This choice is not important for the present analysis.

Assuming that $\mathbf{B}$ is regular (invertible), Equation (11) may be rewritten as

$$c_t^{fs} = -(\mathbf{B}^{-1}\mathbf{A})c^{fs} + b^{fs} \tag{14}$$

Note that $\mathbf{A}$ and $\mathbf{B}$ are sparse matrices. Further, $\mathbf{A} \to \mathbf{0}$ for $\phi^{(0)} \to 0$, and thus the c^{fs}-term on the right-hand side of (14) is left out in the case of no current.

The first-order dynamic free-surface boundary condition (4) is discretized similarly to yield

$$a_t^{fs} = -gc^{fs} - (\mathbf{B}^{-1}\mathbf{C})a^{fs} \tag{15}$$

where

$$\mathbf{C}_{ij} = \frac{\partial \phi^{(0)}(\mathbf{x}_i)}{\partial x}\frac{\partial B_j(\mathbf{x}_i)}{\partial x} + \frac{\partial \phi^{(0)}(\mathbf{x}_i)}{\partial y}\frac{\partial B_j(\mathbf{x}_i)}{\partial y} \tag{16}$$

It is noted that $\mathbf{C} \to \mathbf{0}$ for $\phi^{(0)} \to 0$, and thus the a^{fs}-term on the right hand side of (15) is left out in a zero-current situation.

On the body, on the sea bed and on the truncation boundaries, explicit Neumann boundary conditions of the form (5) are employed. Discretizing these equations yields

$$\mathbf{B}^{(N)}b^N = f(t) \tag{17}$$

where superscripts N denote 'Neumann boundaries' and is not to be confused with the number of basis functions, N, defined previously.

When a collocation method is used, the basis function in (9) can be used to discretize the boundary integral equation (6) as

$$\sum_{j=1}^{N}\left[\left(\alpha(\mathbf{x}_i)B_j(\mathbf{x}_i) + \int_{\Gamma(\xi)} G_n(\mathbf{x}_i, \boldsymbol{\xi})B_j(\boldsymbol{\xi})\,d\Gamma\right)a_j^{(p)}(t)\right] = \sum_{j=1}^{N}\int_{\Gamma(\xi)} G(\mathbf{x}_i, \boldsymbol{\xi})B_j(\boldsymbol{\xi})\,d\Gamma b_j^{(p)}(t) \tag{18}$$

Here $\mathbf{x}_i$ denotes a collocation point located on the boundary Γ. When exactly N collocation points are chosen, (18) forms a square set of algebraic equations which may be written in matrix form as

$$\mathfrak{A}a^{(p)} = \mathfrak{B}b^{(p)} \tag{19}$$

where

$$\mathfrak{A}_{ij} = \alpha(\mathbf{x}_i)B_j(\mathbf{x}_i) + \int_{\Gamma(\xi)} G_{\mathrm{n}}(\mathbf{x}_i, \boldsymbol{\xi})B_j(\boldsymbol{\xi})\,\mathrm{d}\Gamma, \quad i,j = 1, \ldots, N \tag{20}$$

$$\mathfrak{B}_{ij} = \int_{\Gamma(\xi)} G(\mathbf{x}_i, \boldsymbol{\xi})B_j(\boldsymbol{\xi})\,\mathrm{d}\Gamma, \quad i,j = 1, \ldots, N \tag{21}$$

The matrix entries $\mathfrak{A}_{ij}$ and $\mathfrak{B}_{ij}$ are often denoted 'influence coefficients', or 'dipole' and 'source' coefficients respectively.

If the superscript that denotes first-order is omitted, and if the vectors a and b are divided into free surface and Neumann parts, then (19) can be rewritten as

$$\begin{bmatrix} \mathfrak{A}_{11} & \mathfrak{A}_{12} \\ \mathfrak{A}_{21} & \mathfrak{A}_{22} \end{bmatrix} \begin{pmatrix} a^{\mathrm{fs}} \\ a^{\mathrm{N}} \end{pmatrix} = \begin{bmatrix} \mathfrak{B}_{11} & \mathfrak{B}_{12} \\ \mathfrak{B}_{21} & \mathfrak{B}_{22} \end{bmatrix} \begin{pmatrix} b^{\mathrm{fs}} \\ b^{\mathrm{N}} \end{pmatrix} \tag{22}$$

Here the upper matrix blocks correspond to (scalar) boundary integral equations with collocation points on the free-surface boundary. Similarly, the lower blocks correspond to scalar equations on Neumann boundaries.

If it is assumed that $\mathfrak{A}_{22}$ is regular, then the lower block equations in (22) can be rewritten as

$$a^{\mathrm{N}} = -\mathfrak{A}_{22}^{-1}\mathfrak{A}_{21}a^{\mathrm{fs}} + \mathfrak{A}_{22}^{-1}\mathfrak{B}_{21}b^{\mathrm{fs}} + \mathfrak{A}_{22}^{-1}\mathfrak{B}_{22}b^{\mathrm{N}} \tag{23}$$

This is inserted into the free-surface part of (22), i.e. the upper blocks, to eliminate a^{N} from these equations. By assuming that $(\mathfrak{B}_{11} - \mathfrak{A}_{12}\mathfrak{A}_{22}^{-1}\mathfrak{B}_{21})$ is regular, it can be shown that

$$b^{\mathrm{fs}} = \mathbf{D}a^{\mathrm{fs}} - \mathbf{E}b^{\mathrm{N}} \tag{24a}$$

where

$$\mathbf{D} = (\mathfrak{B}_{11} - \mathfrak{A}_{12}\mathfrak{A}_{22}^{-1}\mathfrak{B}_{21})^{-1}(\mathfrak{A}_{11} - \mathfrak{A}_{12}\mathfrak{A}_{22}^{-1}\mathfrak{A}_{21}) \tag{24b}$$

$$\mathbf{E} = (\mathfrak{B}_{11} - \mathfrak{A}_{12}\mathfrak{A}_{22}^{-1}\mathfrak{B}_{21})^{-1}(\mathfrak{B}_{12} - \mathfrak{A}_{12}\mathfrak{A}_{22}^{-1}\mathfrak{B}_{22}) \tag{24c}$$

The boundary conditions (14), (15), (17) and the integral equations (24) can be combined into one set of linear ordinary differential equations (ODEs). When b^{fs} from (24) is inserted in the kinematic free-surface boundary condition (14), then

$$c_t^{\mathrm{fs}} = -(\mathbf{B}^{-1}\mathbf{A})c^{\mathrm{fs}} + \mathbf{D}a^{\mathrm{fs}} - \mathbf{E}b^{\mathrm{N}} \tag{25}$$

Together with the dynamic free-surface boundary condition (15) the system of equations may be written as

$$\frac{\partial}{\partial t}\begin{pmatrix} c^{\mathrm{fs}} \\ a^{\mathrm{fs}} \end{pmatrix} = \begin{pmatrix} -\mathbf{B}^{-1}\mathbf{A} & \mathbf{D} \\ -g\mathbf{I} & -\mathbf{B}^{-1}\mathbf{C} \end{pmatrix}\begin{pmatrix} c^{\mathrm{fs}} \\ a^{\mathrm{fs}} \end{pmatrix} - \begin{pmatrix} \mathbf{E} \\ 0 \end{pmatrix} b^{\mathrm{N}} \tag{26}$$

where $\mathbf{I}$ is the identity matrix. Since b^{N} can be considered as known explicitly (17), (26) can be rewritten in the form normally assumed for a system of linear ODEs

$$\Psi_t = \mathbf{M}\Psi + F(t), \qquad \Psi(t) = \begin{pmatrix} c^{\mathrm{fs}} \\ a^{\mathrm{fs}} \end{pmatrix} \tag{27}$$

Note that the matrix $\mathbf{M}$ is a function of the boundary geometry and discretization, but not a function of the unknowns (Ψ), nor of time. It is possible to use $\mathbf{M}$ directly when integrating the system in time. Unfortunately, the computation of $\mathbf{M}$ is too demanding with respect to CPU time for such a method to be feasible for ordinary applications. However, the system can be analysed for stability by examining the properties (eigenvalues) of $\mathbf{M}$. It is well known that for each (complex) eigenvalue λ of $\mathbf{M}$, (27) has an 'eigensolution' (solution to the homogeneous equation) $\Psi(t) = \Psi(0)\exp(\lambda t)$. Thus, if $\mathbf{M}$ has an eigenvalue with a positive real part, then the corresponding eigensolution will grow exponentially in time, resulting in an unstable solution.

5. DIFFERENCE EQUATION FORMULATION

Following Büchmann [8] a linear multi-step method will be used for time-integrating the free-surface boundary conditions (14) and (15). In particular, the mixed implicit–explicit Euler scheme [9], which is extensively reviewed by Büchmann [8], is chosen for time-integration in the present work. Thus, the kinematic condition (14) is integrated using an explicit Euler scheme, while the dynamic condition (15) is integrated using a (semi-) implicit Euler scheme. The idea behind the mixed Euler scheme is to combine the efficiency of the explicit Euler scheme with the stability of the implicit Euler scheme.

Even though the mixed Euler scheme is used in the present work, this is not a general limitation of the method. Higher-order multistep schemes could well be considered.

At each time step the boundary integral equations (19) are solved to yield the coefficients b_k^{fs} in the form (24). Here, and in the following, subscripts k represent the time levels, i.e. $b_k^{\mathrm{fs}} = b^{\mathrm{fs}}(t = k\Delta t)$. The kinematic free-surface boundary condition (14) is time-integrated using the explicit Euler scheme, i.e.

$$c_{k+1}^{\mathrm{fs}} = c_k^{\mathrm{fs}} + \Delta t[b_k^{\mathrm{fs}} - \mathbf{B}^{-1}\mathbf{A}c_k^{\mathrm{fs}}] \tag{28}$$

Inserting b_k^{fs} obtained through (24) yields

$$c_{k+1}^{\mathrm{fs}} = [\mathbf{I} - \Delta t \mathbf{B}^{-1}\mathbf{A}]c_k^{\mathrm{fs}} + \Delta t \mathbf{D} a_k^{\mathrm{fs}} - \Delta t \mathbf{E} b_k^{\mathrm{N}} \tag{29}$$

Similarly, using the implicit Euler scheme to time-integrate the dynamic condition (15) yields

$$a_{k+1}^{\mathrm{fs}} = a_k^{\mathrm{fs}} + \Delta t[-g c_{k+1}^{\mathrm{fs}} - \mathbf{B}^{-1}\mathbf{C} a_{k+1}^{\mathrm{fs}}] \tag{30}$$

If a_{k+1}^{fs} is isolated, and if c_{k+1}^{fs} from (29) is inserted, then (30) can be rewritten as

$$\begin{aligned} a_{k+1}^{\mathrm{fs}} = & -g\Delta t[\mathbf{I} + \Delta t \mathbf{B}^{-1}\mathbf{C}]^{-1}[\mathbf{I} - \Delta t \mathbf{B}^{-1}\mathbf{A}]c_k^{\mathrm{fs}} + [\mathbf{I} + \Delta t \mathbf{B}^{-1}\mathbf{C}]^{-1}[\mathbf{I} - g\Delta t^2 \mathbf{D}]a_k^{\mathrm{fs}} \\ & + g\Delta t^2[\mathbf{I} + \Delta t \mathbf{B}^{-1}\mathbf{C}]^{-1}\mathbf{E} b_k^{\mathrm{N}} \end{aligned} \tag{31}$$

It should be noted that in the time-domain model, the dynamic condition is not solved explicitly. Rather, the implicit condition is applied to iteratively obtain the solution.

If, rather than time-integrating the coefficients of the basis functions, the physical quantities are time-integrated using (3) and (4), then the same result is obtained. Landrini *et al.* [11] suggest an updating procedure based on the coefficients of the basis functions, while Büchmann *et al.* [4] time-integrate the physical quantities. However, which method is more computationally efficient for practical applications is still undecided.

The system of equations (29) and (31) now is in a standard difference equation form:

$$\Psi_{k+1} = \mathbf{M}^* \Psi_k + F_k, \quad \Psi_k = \begin{pmatrix} c_k^{\mathrm{fs}} \\ a_k^{\mathrm{fs}} \end{pmatrix} = \begin{pmatrix} c^{\mathrm{fs}} \\ a^{\mathrm{fs}} \end{pmatrix}_{t = k\Delta t} \tag{32}$$

with

$$\mathbf{M}^* = \left[\begin{array}{c|c} \mathbf{I} - \Delta t \mathbf{B}^{-1}\mathbf{A} & \Delta t \mathbf{D} \\ \hline -g\Delta t[\mathbf{I} + \Delta t \mathbf{B}^{-1}\mathbf{C}]^{-1}[\mathbf{I} - \Delta t \mathbf{B}^{-1}\mathbf{A}] & [\mathbf{I} + \Delta t \mathbf{B}^{-1}\mathbf{C}]^{-1}[\mathbf{I} - g\Delta t^2 \mathbf{D}] \end{array}\right] \tag{33a}$$

$$F_k = \left[\begin{array}{c} -\Delta t \mathbf{E} \\ \hline g\Delta t^2[\mathbf{I} + \Delta t \mathbf{B}^{-1}\mathbf{C}]^{-1}\mathbf{E} \end{array}\right] b_k^{\mathrm{N}} \tag{33b}$$

If another linear multi-step scheme is chosen, then other values of $\mathbf{M}^*$ and F_k would be obtained. When a higher-order multistep scheme is considered, then the structure of $\mathbf{M}^*$ in (32) becomes more complicated and Ψ_k contains the free-surface coefficients for more than one time step (see e.g. Stoer and Bulirsch [12]).

For each (complex) eigenvalue λ^* of $\mathbf{M}^*$, (32) has an eigensolution, where $\Psi_{k+1} = \lambda^* \Psi_k = (\lambda^*)^k \Psi_1$. The modulus of the eigenvalue corresponds to the magnification of the solution vector per time step taken, while the argument can be related to the period of the solution. Thus, if $\mathbf{M}^*$ has an eigenvalue with modulus larger than unity, then the corresponding

eigensolution will grow exponentially in time, resulting in an instability in the numerical scheme.

6. APPLICATION THE ANALYSIS

As was noted in Section 1, the B-spline-based boundary element model at hand has shown unstable behaviour even in cases where the stability analysis of the discrete dispersion relation [8,9] predicts the model to be stable. In this section the instabilities will be examined in detail in one particular case.

Consider a square wave tank, which is filled such that the water depth, h, equals the length of each side, as shown in Figure 4. Each of the six boundaries in discretized into 8×8 elements of equal size (shown on the figure for the linearized free surface only). Thus, the water depth is $h = 8\Delta x$, where Δx is the mesh size and the panel aspect ratio is $\Delta x/\Delta y = 1$. At the boundaries of each face of the cube, i.e. at the edges of the numerical wave tank, multiple knots, cf. Figure 3, are used to define the B-spline basis. Each basis function is then obtained as a tensor product of two one-dimensional B-splines. When third-order B-spline basis functions (piecewise quadratic polynomials) are chosen, then 100 collocation points are used for each of the six boundaries as shown in Figure 4. A current, defined by the Froude number $F_h \equiv U/\sqrt{gDx} = 0.10$, is applied in one of the two directions parallel to the edges of the free-surface panels, i.e. the current direction does not intersect the free-surface panels at an oblique angle.

Stability analysis of the discrete dispersion relation yields that this setup should result in a stable solution if the time step size, Δt, is chosen such that $\beta \equiv \sqrt{\Delta x}/(\Delta t\sqrt{g}) > 1.05$ [8]. It should be noted that this stability criterion depends neither on the conditions used on the lateral boundaries nor on the initial conditions for the elevation and potential.

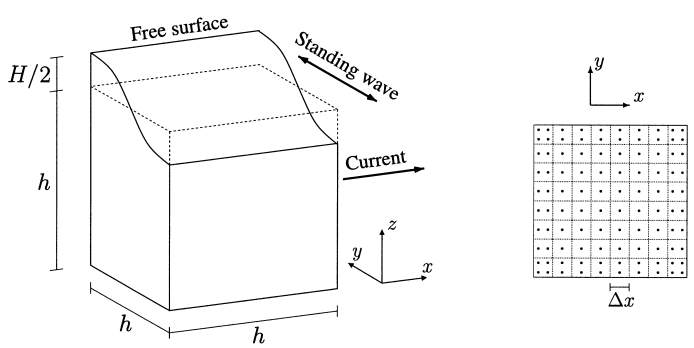

Figure 4. On the left is shown a sketch of the basic example used in the present work: a standing wave superimposed on a perpendicular current in a regular wave tank. The side lengths of the wave tank equal the mean water depth, h. The dotted lines represent the time-invariant linearized geometry. On the right is shown the discretization of the linearized free surface, which is divided into 8×8 elements (- - -). Also shown are the 10×10 collocation points (●) positioned at the centroids of the basis functions (third-order B-splines used).

For the first-order velocity potential, homogeneous Neumann conditions are applied on the sea bed and at the truncation boundaries. Since no energy is supplied through these boundaries or through the free surface, the first-order problem has zero external forcing. To initiate the calculations a standing wave is started from rest, with adjacent anti-nodes located at two of the lateral boundaries (see Figure 4). Thus, the wave length, L, equals twice the width of the wave tank, $L = 2h = 16\Delta x$, corresponding to a non-dimensional wave number $kh = \pi$. The wave propagation is chosen perpendicular to the current direction, such that the current does not affect the period and the shape of the wave.

Time series of the water elevation have been recorded at the collocation point closest to the corner of the free surface. These results have, for three different time step sizes ($\beta = 10$, 20 and 50), already been shown in Figure 1. It is seen that the model is unstable for all three time-step sizes, even though the stability analysis of the discrete dispersion relation predicts the model to be stable for these values of β. It is noticed from Figure 1 that the three simulations all show exactly the same instability behaviour. In fact, as the time step size is decreased, the model converges to a solution that is unstable in time. A longer simulation reveals that the instabilities grow exponentially in time (see Figure 5). This instability constitutes a discrepancy between the stability analyses [8,9], which predict the model to be stable, and the actual model behaviour. It is recalled that in order to make a stability analysis a set of assumptions is made, see Section 2. Most importantly, it is assumed that the free surface is of infinite extent in all horizontal directions and that the discretization is uniform. Thus, all effects of truncation boundaries, fixed or floating bodies and non-uniform basis functions have been ignored. Thus, when the result from the stability analysis is interpreted, it is important to note that the stability criterion obtained ($\beta > 1.05$) is a necessary, but obviously not sufficient, condition for stability.

Since the instabilities grow exponentially in time, it is possible to estimate the eigenvalue with largest modulus from a long time series (see Figure 5). This procedure corresponds closely to finding eigenvalues by using the so-called 'power method'. Comparison can then be made with the eigenvalues of $\mathbf{M}^*$ in (32) obtained using a difference equation formulation. In this particular case the eigenvalues of $\mathbf{M}^*$ with maximum modulus are very closely spaced (see

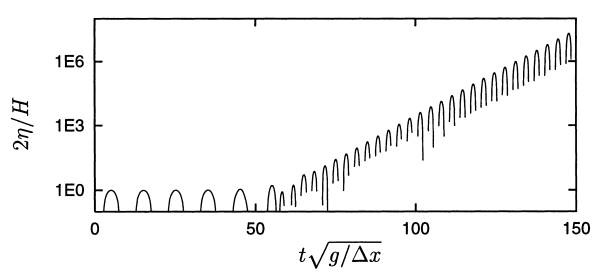

Figure 5. Time series of elevation at a particular collocation point using $\beta = 10$ showing a pronounced temporal instability. The results correspond exactly to the data for $\beta = 10$ shown in Figure 1. The broken (discontinuous) nature of the curve is due to the removal from the time series of all values of negative sign.

Table I). Thus, the eigenvalue obtained from the time series may depend on the amount of energy initially being in each eigensolution. In the present case, the time series follows closely the eigensolution corresponding to the eigenvalue with second largest modulus. If the initial conditions are changed to a current direction parallel to the standing wave profile, then the eigensolution corresponding to the eigenvalue with largest modulus is obtained. In principle the 'largest eigensolution' will dominate if time gets large enough (independent of the initial conditions), but that may not happen before an computational overflow is encountered. As can be seen from Figure 6, a comparison of the surface elevation obtained from the

Table I. The four conjugated pairs of eigenvalues with largest modulus found by numerically solving the eigenvalue problem $\mathbf{M}^*\mathbf{v} = \lambda^*\mathbf{v}$ obtained from (32).

Eigenvalue pair number	Eigenvalue	
	Modulus	Argument
1	1.0186665	± 0.1892239
2	1.0186002	± 0.1899729
3	1.0185307	± 0.1917973
4	1.0184384	± 0.1947614
$(*)$	1.01860	± 0.19072

The eigenvalue ($\lambda^*_{(*)}$) estimated from the time series in Figure 5 is also given $(*)$. The results are for the chosen model problem with $F_h = 0.10$ and a time step size corresponding to $\beta = 10$.

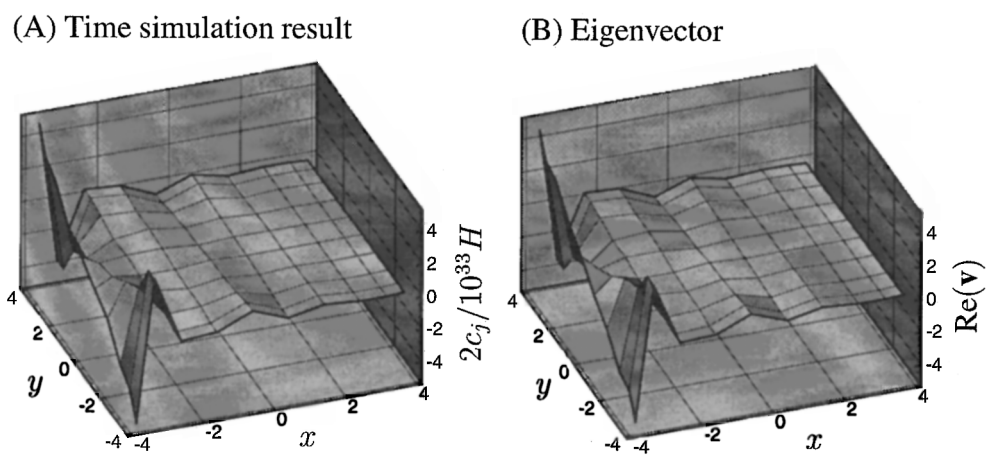

Figure 6. Coefficients c_j (9) for the elevations at the free surface plotted at the collocation points (basis function centroids). (A) results from an unstable time domain simulation, and (B) the real part of an eigenvector $\mathbf{v}$ corresponding to the eigenvalue of $\mathbf{M}^*$ in (32) with second largest modulus (see Table I). Due to the properties of the B-spline basis, the wave elevation η to a high degree shares the same features as the plotted coefficients.

time-domain model (for a large value of t) with the eigenvector (eigensolution) corresponding to the eigenvalue with second largest modulus shows very good agreement. In Figure 6, the coefficient c_j of each basis function on the free surface has been plotted at the collocation point corresponding to the centroid of the basis function. Also shown is an eigenvector corresponding to the eigenvalue with second largest modulus. The eigenvector has been calculated using LAPACK [13] and has been scaled by a complex constant to give maximum similarity with the time series result. It is obvious from Figure 6 that the eigensolution contains almost all the energy in the time-domain result, thus confirming that the instability is caused by the aforementioned eigenvalue.

In order to eliminate all effects of the time integration scheme, the system of linear ODEs (27) is considered. As mentioned, for each (complex) eigenvalue λ of $\mathbf{M}$, (27) has an eigensolution $\Psi(t) = \Psi(0)\,\mathrm{e}^{\lambda t}$. For the present model case the eigenvalues of $\mathbf{M}$ have been found numerically (see Figure 7). The eigenvalues with negative real part, corresponding to temporally damped eigensolutions, are not shown. The shown eigenvalues have zero or positive real parts, corresponding to eigensolutions which are respectively, periodic or unstable in time. Since $\mathbf{M}$ has only real entries, the eigenvalues with negative imaginary part can be obtained as complex conjugates of the shown eigenvalues. If the eigenvalue with second largest real part ($\lambda\sqrt{\Delta x/g} = 0.1842960 \pm \mathrm{i}1.8969$) is examined more closely, the expected unstable solution can be obtained once again. In particular, the growth rate over one non-dimensional time unit $\sqrt{\Delta x/g}$ is $\exp(\sqrt{\Delta x/g}Re\lambda) = 1.20237$. From the time series using $\beta = 10$ there are $\sqrt{\Delta x/g}/\Delta t = \beta = 10$ time steps per non-dimensional time unit. Thus, the observed growth per time unit in the time series can be obtained as $(\lambda^*_{(*)})^\beta = 1.0185984^{10} = 1.20235$, which is very close to the formerly found result (see also Table I). Also, the angular frequency of the instability $\sqrt{\Delta x/g}\,\mathrm{Im}(\lambda) = 1.8969$ agrees fairly well with the time series estimate $\beta\arg(\lambda^*_{(*)}) = 10 \times 0.19072 = 1.9072$. Thus, it is evident that the instabilities observed in the time series (see Figure 1) are not a feature of the chosen time integration scheme, but are actually a property of the spatially discretized equations. Consequently, for the chosen time-integration scheme, there does not exist a Courant condition for this type of instability: the instability will persist

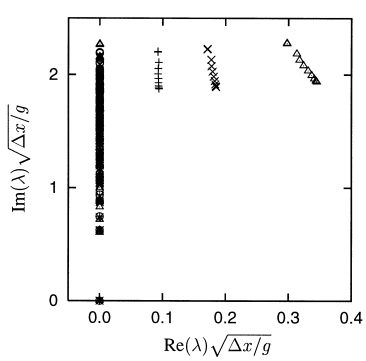

Figure 7. Eigenvalues of $\mathbf{M}$ in (27) for the chosen model problem and $F_h = 0.00$ (○), 0.05 (+), 0.10 (×), and 0.20 (△).

even as $\Delta t \to 0$. Thus, rather than obtaining a stable result, the model will converge temporally to a solution which is unstable in time. When other time integration schemes are chosen, such as higher-order Adams or Runge–Kutta schemes, the same instabilities have been observed (results not shown). It should be noted for completeness that the zero eigenvalues of **M** observed in Figure 7 correspond to eigensolutions which are constant in time. Obviously, the eigenvectors in this case correspond to solutions with constant elevation and potential in space, i.e. a change of the mean water level and potential.

From Figure 7 it is further observed that the largest real part of the eigenvalues of **M** scales roughly linearly with the Froude number F_h. In fact, no instabilities are expected when $F_h = 0$.

In the present case the largest magnitude of the eigenvalues scales roughly with the inverse of the grid size (results not shown). Thus, if the grid is refined, then the instabilities increase in both frequency and growth rate. However, if the time step size is decreased also, such that $\Delta t/\Delta x$ does not increase, then the growth rate per time step remains bounded. It should be noted, though, that this criterion on the time step size may result in much smaller time steps than the Courant type stability criterion $\beta \geq \beta_c$ obtained by the former stability analysis [8,9], whereby $\Delta t \sim \sqrt{\Delta x}$.

In the following $\lambda^*_{\max}$ will denote that eigenvalue of M^*, which has maximum modulus. Thus, $\lambda^*_{\max}$ dominates the model behaviour in the unstable situations as discussed previously. The modulus and argument (phase) of $\lambda^*_{\max}$ have been examined for varying time step sizes, see Figure 8. In a zero current situation, the modulus of $\lambda^*_{\max}$ drops to unity very close to the critical value of β predicted by the traditional stability analysis, cf. figure 6 in Büchmann [8], such that the method is stable for large values of β. For low values of β the scheme is unstable and the argument of the dominant eigenvalue is π. Therefore, for the unstable solution, the sign changes at every time step, in a manner known from the classical 'saw-tooth instabilities'. In other words, this instability is occurring on the temporal Nyquist frequency and will be very obvious if a time series is examined. The cause of this instability is that a 'stable' eigenvalue of M, e.g. λ having zero real part, lies outside the stability region of the chosen time integration scheme. Seemingly, this kind of instability is predicted very well by the existing stability analysis [8,9].

If a current is introduced, then important changes take place in the stability behaviour of the scheme. For low values of β the stability is still dominated by the classical saw-tooth type instability. However, when β is increased and the modulus of this type of eigenvalue drops to unity, then a second type of instability takes over (see Figure 8). From the figure, it is immediately noted that this second instability is of a quite different nature than the classical saw-tooth instability. For instance, as the time step size is decreased, this second instability will not be of high frequency compared with the time scale of Δt. Thus temporal filtering may not be used to suppress these instabilities. Fortunately, as can be seen in Figure 6, the instabilities occur for a wave number close to the spatial Nyquist frequency. Thus, spatial filtering may be used to effectively suppress these instabilities. As has been shown previously, this kind of instability is caused by an initially 'unstable' eigenvalue of M, i.e. λ having positive real part.

Some time integration schemes, such as the purely implicit Euler scheme, have the property of stabilizing eigensolutions corresponding to eigenvalues in certain parts of the positive real half plane. However, these schemes are often implicit in type, requiring several solutions of the boundary integral equations at each time step. As a consequence, these methods may well be

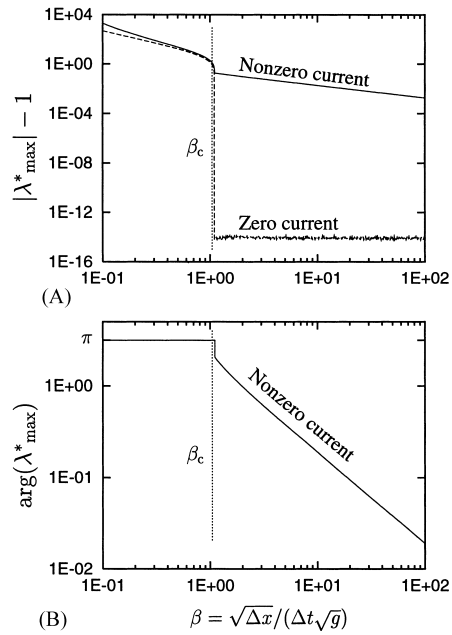

Figure 8. Behaviour of the eigenvalue, $\lambda^*_{\max}$, with largest modulus for varying time step size in the test case. Variation of the modulus (A) and the argument in those cases where $\lambda^*_{\max} > 1$ (B). Results are given for $F_h = 0.00$ (– – –) and for $F_h = 0.10$ (—). The theoretical limit [8,9] for stability $\beta_c = 1.05$ is shown with dots.

too demanding with respect to computing time. Also, since the stability analysis did not predict this kind of instability, a new stability analysis that includes the non-uniformity of the free surface as well as Neumann boundary effects needs to be made, in order to find a stability criterion for these methods in connection with the time-domain BEMs. Obviously, such an analysis will be very complicated in general and is considered well beyond the scope of the present work. As an alternative, the eigenvalues of **M** in (27) may be considered (see e.g. Figure 7), and compared with the stability region of any well-known time integration scheme.

Finding the eigenvalues of **M** in (27) to obtain a stability criterion for each particular discretization at hand may be possible, but this alternative is clearly very expensive in CPU time and is not feasible for studying the stability in practice. Even though the eigenvalue problem in a global sense, as laid out in the present work, is the proper way to describe the stability of a model, the eigenvalue problem may, in principle, be considered in a localized sense, as mentioned by Kim in the discussion of an abstract by Büchmann and Skourup [14]. However, in a modern BEM using an accelerated iterative solution technique, such as the precorrected-FFT method [15], the localized problem may already be used for preconditioning the integral equation. In this setting, finding the eigenvalues of the local problem may yield approximate information on the temporal stability of the fully discretized model in a fashion that is computationally feasible.

7. CONCLUSIONS

A method has been developed for studying the temporal stability of some perturbation-based free-surface boundary element models. The combined equation have been brought to standard difference equation and differential equation formulations in order to examine the stability of the fully discretized and the spatially discretized system of equations. The numerical models in the present work use B-spline basis functions and a mixed implicit–explicit Euler scheme for the spatial and temporal discretization respectively. However, with minor modifications it should be possible to examine also other spatial and temporal discretizations using the present method.

In a practical example, observed instabilities were not predicted by the stability analyses give by Vada and Nakos [9] and by Büchmann [8]. It was found that these instabilities are due to non-uniformities in the employed spatial discretization. These non-uniformities are not taken into account in traditional stability analyses [8,9]. As a consequence, results from these stability analyses should be considered as necessary, but not sufficient, conditions for the stability of a particular model.

It has been suggested by Vada and Nakos [9] and by Kim *et al*. [7] that the instabilities observed in their models are caused by energy from the external forcing, which should be accumulated on a wave number with zero group velocity, a so-called resonant mode. However, this argument fails to explain the observed exponential growth of the instabilities in time. Further, as demonstrated in the present work, instabilities may occur also in situations with zero external forcing. Based on the observations made here, it is conjectured that the instabilities are in fact due to non-uniformity effects in the spatially discretized models—these effects not being included in the respective stability analyses.

If the eigenvalue problem is considered in a localized sense, then approximate information might be obtained on the global stability properties resulting from a particular spatial discretization. If a sparsified BEM, such as the precorrected-FFT method, is used, then local problems may already be solved to precondition the problem, and thus the solution of local eigenvalue-problems may be computationally tractable. The investigation of such a method is left for future work.

ACKNOWLEDGMENTS

This work was sponsored by the Danish Ministry of Education. Their support is greatly appreciated.

REFERENCES

1. Longuet-Higgins MS, Cokelet ED. The deformation of steep surface waves on water, I. A numerical method of computation. *Proceedings of the Royal Society of London*, *Series A* 1976; **350**: 1–26.
2. Dommermuth DG, Yue DKP. Numerical simulation of nonlinear axisymmetrical flows with a free surface. *Journal of Fluid Mechanics* 1987; **178**: 195–219.
3. Isaacson M, Cheung KF. Time-domain second-order wave diffraction in three dimensions. *Journal of Waterway*, *Port*, *Coastal*, *and Ocean Engineering* 1992; **118**(5): 496–516.
4. Büchmann B, Skourup J, Cheung KF. Run-up on a structure due to second-order waves and a current in a numerical wave tank. *Applied Ocean Research* 1998; **20**(5): 297–308.

5. Harten A, Efrony S. A partition technique for the solution of potential flow problems by integral equation methods. *Journal of Computational Physics* 1978; **27**: 71–87.
6. Fleron P. Calculation of hydrodynamic coefficients for a cylinder oscillating in the free surface of restricted water. Technical Report TR-NR 33.560-77094, Danish Maritime Institute, Kgs. Lyngby, Denmark, 1979.
7. Kim Y, Kring DC, Sclavounos PD. Linear and nonlinear interactions of surface waves with bodies by a three-dimensional Rankine panel method. *Applied Ocean Research* 1997; **19**(5/6): 235–249.
8. Büchmann B. Accuracy and stability of time-domain boundary element models based on B-splines. *International Journal for Numerical Methods in Fluids* 2000; **33**: 125–155.
9. Vada T, Nakos DE. Time-marching schemes for ship motion simulations. In *Proceedings of the 8th International Workshop on Water Waves and Floating Bodies*, St. John's, Newfoundland, Canada, Pawlowski JS (ed.). National Research Council Canada: Ottawa, 1993; 155–158.
10. Büchmann B. Time-domain modelling of run-up on offshore structures in waves and current. PhD thesis, Department of Hydrodynamics and Water Resources, Technical University of Denmark, Lyngby, Denmark, 1999. Series Paper No. 71, 1999 http://www.buchmann.dk/bjarne/publicat/phd.html [access date 1 November 2000].
11. Landrini M, Grytøyr G, Faltinsen OM. A B-spline based BEM for unsteady free-surface flows. *Journal of Ship Research* 1999; **43**(1): 13–24.
12. Stoer J, Bulirsch R. *Introduction to numerical analysis* (2nd edn). In *Texts in Applied Mathematics*, vol. 12. Springer-Verlag: New York, 1993 (corrected 3rd printing, 1996).
13. Anderson E, Bai Z, Bischof C, Demmel J, Dongarra J, Du Croz J, Greenbaum A, Hammarling S, McKenney A, Ostrouchov S, Sorensen D. *LAPACK User's Guide* (2nd edn). Society for Industrial and Applied Mathematics: Philadelphia, PA, 1995.
14. Büchmann B, Skourup J. Stability of time-domain boundary element models; theory and applications. In *Proceedings of the 14th International Workshop on Water Waves and Floating Bodies*, Port Huron, Michigan, USA, Beck RF, Schultz WW (eds). University of Michigan Press: Ann Arbor, 1999; 13–16 (discussions in separate volume).
15. Kring D, Korsmeyer T, Singer J, White J. Analyzing mobile offshore bases using accelerated boundary-element methods. *Marine Structures* 2000; **13**: 301–313.

